POLITECNICO DI TORINO
Repository ISTITUZIONALE

Stress and Failure Onset Analysis of Thin Composite Deployables by Global/Local Approach

Original
Stress and Failure Onset Analysis of Thin Composite Deployables by Global/Local Approach / Augello, R.; Pagani, A.; Carrera, E.; Iannotta, D. A.. - In: AIAA JOURNAL. - ISSN 0001-1452. - STAMPA. - 60:10(2022), pp. 5954-5966. [10.2514/1.J061899]

Availability:
This version is available at: 11583/2972172 since: 2022-10-09T17:54:46Z

Publisher:
AMER INST AERONAUTICS ASTRONAUTICS

Published
DOI:10.2514/1.J061899

Terms of use:

This article is made available under terms and conditions as specified in the corresponding bibliographic description in the repository

Publisher copyright

(Article begins on next page)

17 April 2024

Detailed stress state and failure onset analysis of thin composite deployable booms by CUF-based global/local approach

R. Augello*, A. Pagani†, E. Carrera‡ and D. A. Iannotta§
Department of Mechanical and Aerospace Engineering, Politecnico di Torino, 10129, Torino, Italy

The purpose of this work is to propose an innovative global/local approach for the failure onset analysis of deployable composite thin and ultra-thin structures. The adoption of this technique allows for the overcoming of the weaknesses related to the commercial calculation codes, which make use of three-dimensional finite elements to capture the local stress field arising within the booms. In this framework, the proposed approach leads to a reduction of computational cost, while keeping a high level of accuracy. This is possible thanks to the Carrera Unified Formulation, which allows for the modeling of higher-order plate elements for the analysis of local critical regions of complex composite assemblies. In order to show the potentialities of the global/local approach, particular attention is given to the problems that mostly characterize composites, among which those related to free-edge, failure concept and interlaminar continuity of the displacements and shear stresses. The analyzed booms are the triangular rollable and collapsible, a tape-spring hinge and a telescopic tubular mast. The results show a perfect accuracy of the in-plane stress components and an accurate description of the out-of-plane components, which is essential for a reliable design of these components, in terms of free-edge debonding and failure phenomena.

Nomenclature

$\mathbf{D}$	=	linear differential operator
$\mathbf{l}$	=	1D cubic Lagrange polynomial
$\mathbf{L}$	=	2D cubic Lagrange polynomial
E	=	Young modulus
F_τ	=	expansion functions along the thickness coordinate z
$\mathbf{K}^{ij\tau s}$	=	fundamental nucleus of the stiffness matrix
L_{ext}	=	work by external loads

*Postdoc, Department of Mechanical and Aerospace Engineering, Politecnico di Torino, riccardo.augello@polito.it.
†Associate Professor, Department of Mechanical and Aerospace Engineering, Politecnico di Torino, alfonso.pagani@polito.it.
‡Full Professor, Department of Mechanical and Aerospace Engineering, Politecnico di Torino, erasmo.carrera@polito.it.
§Research Assistant, Department of Mechanical and Aerospace Engineering, Politecnico di Torino, s277952@studenti.polito.it

L_{int}	=	internal work
N_i	=	shape function
$\mathbf{q}_{\tau i}$	=	finite element nodal unknowns
u_x^0, u_y^0, u_z^0	=	nodal displacements of the global model
$\theta_x^0, \theta_y^0, \theta_z^0$	=	nodal rotations of the global model
δ	=	variation
ϵ	=	strain vector
σ	=	stress vector
V	=	local volume
Ω	=	local surface

I. Introduction

During the last decades, the size of components and, in general, of space systems, has undergone a significant reduction. In order to support this trend, characterized by an increasing process of miniaturization, the space industry has been oriented towards the development of new methods of volume minimization, which would allow facilitating the development of small satellites [1]. In fact, it is expected that in the future this category of satellites will be able to acquire better performances than those of larger satellites. While the size of avionics and onboard instruments has shrunk, some satellite components, which require the collection or reflection of photons or electromagnetic radiation, must necessarily remain large (e.g. solar panels, communication antennas, and solar sails)[2]. To meet these needs, deployable booms have been introduced.

Deployable booms are folded through a rolling mechanism and can be deployed to acquire a rod-like shape through a system reminiscent of a tape measure. Generally, these structures present a curved cross-section in their unfolded configuration and this feature allows to increase the stiffness of the boom. On the other hand, when rolled up, these structures become curved in the longitudinal direction, while the cross-section flattens out. They found a large number of applications such as for telescopes [3, 4], photovoltaic surfaces [5, 6], antennas [7], solar sails and arrays [6, 8, 9] and advanced aircraft structures [10].

The most common type of deployable booms is represented by tape springs. Basically, they consist of thin-walled elastic strips, whose cross-section forms an arc of a circle. Tape springs exhibit highly nonlinear behavior when stressed with a bending moment. This trend can be evidenced both by experimental tests and by numerical analyses. An abrupt change in the geometry of the structure is observed when the applied moment assumes critical values, as indicated by Seffen and Pellegrino [11]. Tape springs, moreover, are able to unfold due to the release of elastic deformation energy stored in their folded configuration. These structures are stored in the folded configuration for a long time, and

so there is generally viscoelastic relaxation that leads to a reduction in the stored elastic energy and thus an increase in the stability of the system [12, 13]. Tape-springs are widely adopted for a large number of applications, including high-resolution deployable telescope [14] and the deployment of collapsible rib-tensioned surface [15] and rigid-panels [16]. Tape springs can be exploited to generate other types of structures, such as tape-spring hinges [17–19]. The utility of these structures has already been highlighted in a variety of space missions (for instance during the ESA Mars Express mission, a tubular tape-spring hinge was used to implement the Mars Advanced Radar for Subsurface and Ionosphere Sounding (MARSIS) antenna deployment system).

Another type of deployable booms, are Storable Tubular Extendible Members (STEMs) [20–22]. Invented in Canada in 1960, they are similar to tape springs, with the difference that they subtend a greater angle compared to the latter, forming a tubular structure, characterized by an overlap of 50° or more. A further variant is represented by Collapsible Tube Mast (CTM), consisting of two thin flexible shells of biconvex shape bonded at the edges by resistance welding. The thickness of all these structures is sufficiently small to guarantee a purely elastic deformation when folded and, of course, the storage of a large amount of elastic deformation energy in the folded configuration. It is necessary to ensure that this energy is released in a controlled manner during deployment [23]. This type of boom was first adopted during the Viking 1 and 2 [24] robotic explorations, which goal was to collect samples of the soil on the Mars surface.

Another popular deployable boom is represented by the Triangular Rollable And Collapsible (TRAC) boom [25]. It was invented by researchers at the US AirForce Research Laboratory more than ten years ago and it is characterized by a cross-section consisting of two curved flanges connected at their upper edge by a vertical septum, in order to generate a shape similar to that of a triangle (hence the name of the boom). This type of boom has been used in three different missions to perform demonstrations related to solar sails: NanoSail-D [26], LightSail-1 [27] and LightSail-2 [28]. Despite having a rather limited torsional stiffness due to the open section of the structure, TRAC booms are characterized by a flexural stiffness 10 times higher than CTM booms and 34 times higher than STEM booms and packaging efficiency compared to CTM, STEM [29] and bi-STEM booms [30] solutions.

Deployable booms always consist of thin and, eventually, ultra-thin structures [31]. Due to their geometry and due to the anisotropy of the composite material which booms are usually made of, during deployment complicated three-dimensional (3D) stress fields arises within a localized area of the structure, as the interlaminar debonding [32–34]. For this reason, higher-order models and 3D elements are required in order to describe the complex stress fields. These models would request a strong computational effort and a global/local technique can be recalled to increase their efficiency in terms of reliability of the results and time required for the simulation. In literature, two types of global/local procedures were presented, i.e. (1) a single step which involves the refinement of particular domains of the structure and (2) a two-step approach where different areas are analyzed employing different mathematical descriptions. The main issue of the former is represented by the coupling of lower- and more-refined zones subdomains of the structure. According to how the mathematical models differ, the *so-called* h-adaption [35] and p-adaption [36] methods can

be used whit different mesh sizes and different polynomials order functions, respectively. When a combination of those differences is present within the model, the hp-adaption [37] approach can be exploited. Other approaches were proposed as single step global/local procedure, such as the parallel processing [38], the extended finite element method [39] and the multi-grid method [40]. A worth-mentioning approach is represented by the s-version [41, 42] of the finite element method, where additional higher-order elements are superimposed between the two domains. This technique ensures the equilibrium of stresses and the compatibility of displacements at the interface. Finally, the Arlequin method was first proposed by Ben Dhia [43] and then employed by Hu *et al.* [44] for the analysis of sandwich beams.

As far as the two-step approaches are concerned, they consist in an analysis of the global structure, from which the boundary conditions of the critical region are extracted. Usually, these boundary conditions are represented by the displacements, as done by Akterskaia *et al.* [45] for the progressive failure analysis of composite structures, by Mao *et al.* [46] which considered a region larger than the critical one where accurate stresses need to be evaluated in order to avoid any kind of numerical issues. Moreover, stress analyses were conducted by Ransom and Knight [47], using spline interpolation functions and simply supported composite plate with cutouts and small cracks were analyzed in cutouts [48] and [49], respectively.

The presents work proposes a global/local approach based on a two-step procedure in which the global analysis is at first performed using commercial software Nastran and subsequently a local area is analyzed using refined theories with CUF formalism. In fact, CUF models have been demonstrated to be very efficient and effective for evaluating complex strain/stress fields of composite structures [50, 51] and also successful in the elastoplastic and progressive failure analyses [52, 53]. The same global/local approach proposed in this paper was employed in [54, 55] for the analysis of structure of aeronautic interest, and here the formulation is further extended to deal with composite deployable booms. Recently, CUF has been extended in [56] to deal with the global/local analysis of laminates by employing its intrinsic variable-kinematics capability. Finally, application of CUF for the nonlinear analysis of booms can be found in [57–59].

II. Global/local approach

The global/local strategy adopted and proposed in this paper consists in two steps, which can be summarized in

1 **A global analysis is conducted considering the whole deployable boom.** In this work, the global analysis is conducted using the commercial software Nastran. Due to the thinness of the considered booms, CQUAD elements are adopted, along with PCOMP cards for the description of the geometric and material properties [60]. The global analysis is important especially for the identification of the most critical zones which need further and more refined investigation. To detect those domains, the maximum stress is considered, but any criteria can be conducted with no loss of generality. It has to be remarked that the proposed approach is element-wise, so that one element (one CQUAD) at a time is locally analyzed.

2 **A local analysis is performed on the selected element.** Subsequently, a local model of the selected element is

built. Figure 1 shows an example of this procedure on a tubular thin-walled boom.

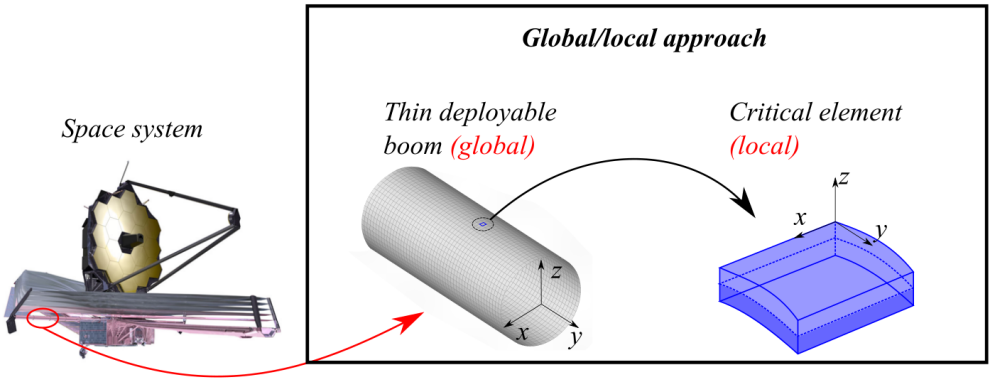

Fig. 1 Application of the two-step global/local approach on a thin deployable boom of a space system.

A. Higher-order two-dimensional local model

The local model is built using higher-order 2D plate theory based on CUF [51, 61], according to which, the 3D local displacement field $\mathbf{u}(x, y, z)$ can be expressed as a 1D through-the-thickness (z) expansion function of the primary unknowns of the mid-surface (x, y) evaluated with the finite element method. This approach is expressed by the following relation

$$\mathbf{u}(x, y, z) = F_\tau(z) N_i(x, y) \mathbf{q}_{\tau i} \tag{1}$$

where F_τ is the expansion function, N_i is the finite element shape function, $\mathbf{q}_{\tau i}$ is the vector of the nodal unknowns and the indices τ and i represent the number of the terms of the thickness expansion and the number of the the finite element nodes, respectively. In this work, cubic interpolation functions based on Lagrange polynomials are used as F_τ and N_i, as depicted in Fig. 2. In this work, the cubic interpolation over the thickness is recalled as LD3. It must be stated that Lagrange polynomials represent a displacement-based formulation, so the unknowns of the local problem are pure displacements. A detailed description of the modeling of the local model is proposed in Appendix A.

B. Boundary conditions

As known, the commercial software gives translational displacements (u_x^0, u_y^0, u_z^0) and rotations $(\theta_x^0, \theta_y^0, \theta_z^0)$ at the each node of the global model. On the other hand, as previously mentioned, the use of Lagrange polynomials results solely in pure displacement degrees of freedom (DOFs) at each over-the-thickness node. Therefore, a strategy must be provided to transform rotational DOFs of the global model in pure displacements for local one. Reissner-Mindlin displacement field is used for the 2D model, in order to compute the translational displacements for each node at the

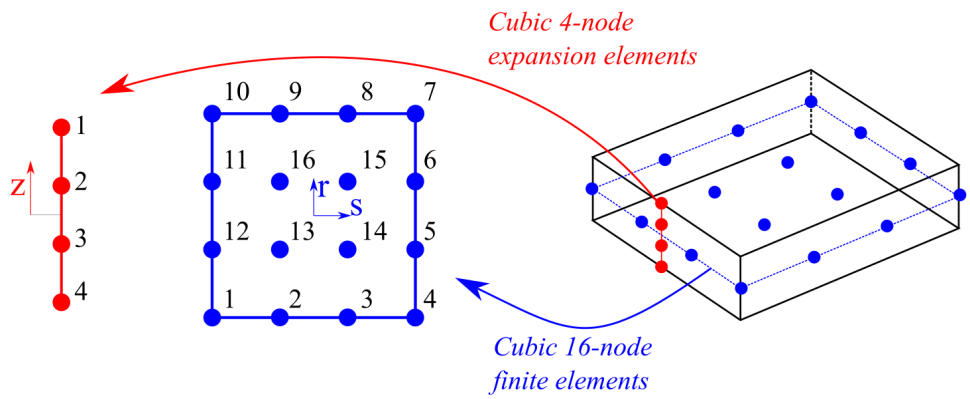

Fig. 2 Cubic interpolations for the in-plane and thickness domains.

interface of the CUF local model. The Reissner-Mindlin displacement field [62, 63]) is reported in Eq. (2) and Fig. 3.

$$
\begin{aligned}
u_x(x,y,z) &= u_x^0(x,y) + z\theta_y^0(x,y) \\
u_y(x,y,z) &= u_y^0(x,y) + z\theta_x^0(x,y) \\
u_z(x,y,z) &= u_z^0(x,y)
\end{aligned}
\tag{2}
$$

In Eq. (2), u_0, v_0, w_0 are the displacements and $\theta_x, \theta_y, \theta_z$ are the rotations of the nodes of the global model located at

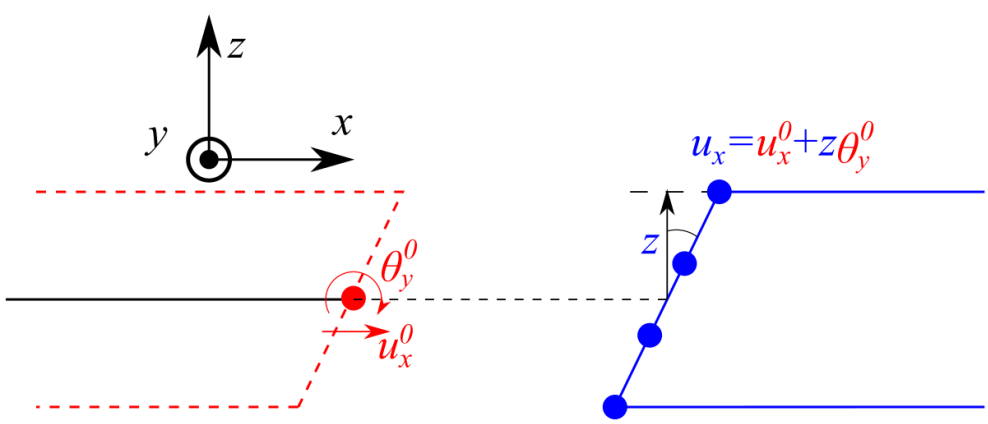

Fig. 3 Global to local displacement field in the laminated plate thickness.

the interface. The rotations are used to compute displacements in all the edge nodes and they constitute the BCs for the local model. Figure 4 depicts the general procedure.

III. Numerical results

In this section, numerical results obtained with the presented global/local approach are proposed. A TRAC boom, a tape-spring hinge and a Telescopic Tubular mast are considered. Stresses distributions, free-edge effects and failure

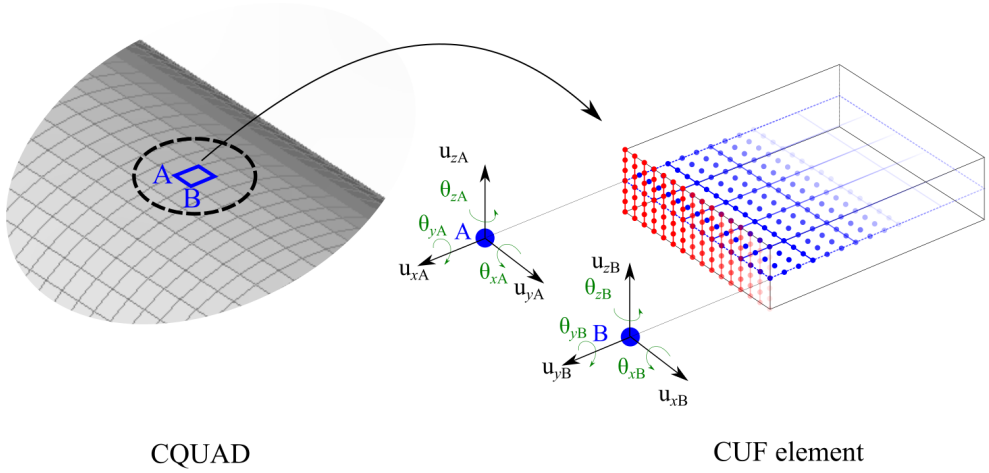

Fig. 4 Procedure to transform rotational DOFs of the global model in pure displacements for local one.

indeces are evaluated. The local in-plane stresses are compared to those evaluated with 2D CQUAD Nastran elements, and they are reported in the global and material reference system, which are denoted by index "G" and "M", respectively.

A. TRAC boom

The first analysis regards a deployable TRAC boom [64]. The geometrical model, along with the material stacking sequence, is shown in Fig. 5. Basically, the structure is made of two curved flange, joined together by a flat vertical web. In particular, the radius is r = 12.7 mm, the sweep angle θ = 90, h = 8 mm and the total length of the boom is 500 mm. The material is made of Carbon Fiber (CF) and Glass Fiber Plain Weave (GFPW). The curved flanges are made of three

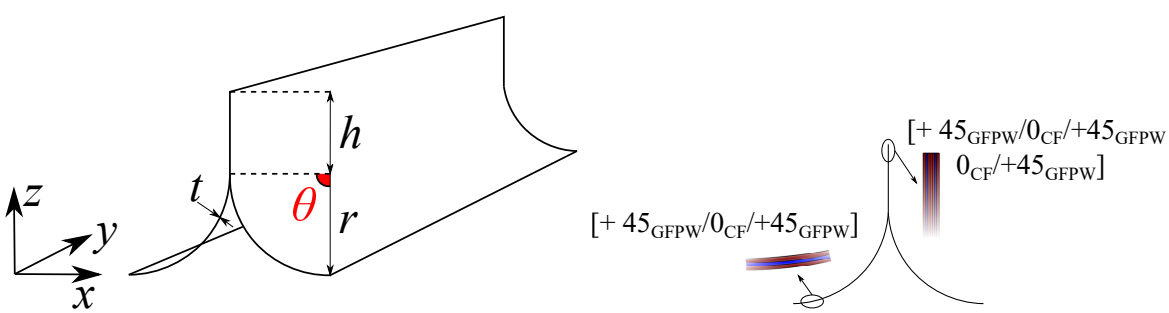

Fig. 5 Geometric and material properties of the deployable TRAC boom.

layers and have thickness equal to 80 μm, whereas the vertical web has seven layers, with a total thickness of 185 μm. The material properties are described in Table 1. The global Nastran model is performed following the description reported in [64], where the mathematical approximation is validated. The model involves 11000 CQUAD, with a total of 70794 DOFs and it is simply supported. The structure is loaded by a moment M_x, considered positive when the vertical web is under compression and the results are shown in Fig. 6, where the results are compared with those from experiments [64] and numerical nonlinear analysis [65]. Here, the rotation angle α_x is displayed against the applied

	E_1 [GPa]	E_2 [GPa]	G_{12} [GPa]	ν_{12} [-]	t_{layer} [μm]
CF	128	6.5	7.6	0.35	30
GFPW	23.8	23.8	3.3	0.17	25

Table 1 Material properties of the TRAC boom.

moment M_x.

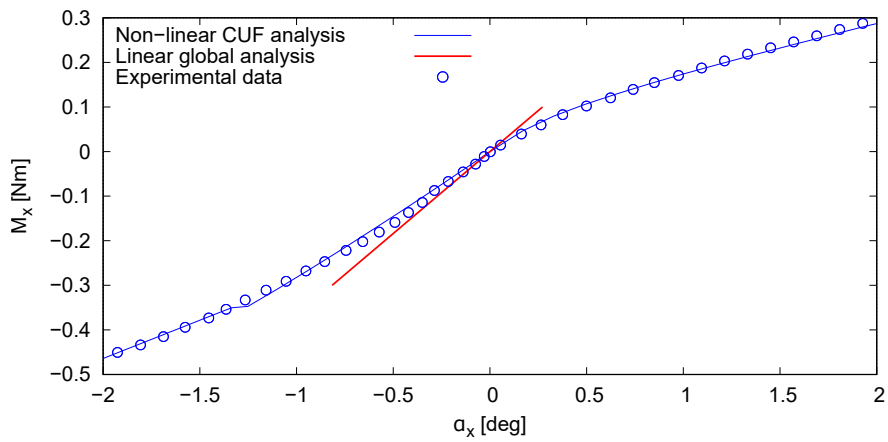

Fig. 6 Rotation angle α_x of the TRAC boom against the applied moment M_x. Linear analysis compared to experimental results [64] and numerical nonlinear solution [65].

1. Local analysis

The local analysis is performed starting from the global results applying $M_x = 100$ Nmm. The chosen elements are those which are subjected to the highest stress value, and they are reported in Fig. 7. The two chosen elements lay on the free-edge of the vertical web (compression) and the curved flange (traction), respectively. Figure 7(b) shows the chosen elements, i.e. element A on the vertical web and element B on the curved flange. As far as the element A is concerned, the stress distributions are reported for both global and material reference system. The results are shown in Figs. 8 and 9. On the material reference system, for the in-plane stress components, the local results are compared with the global ones, and the results match with a great accuracy. Regarding the element B, the stress distributions are reported for both global and material reference system. The results are shown in Figs. 10 and 11.

2. Free-edge analysis

Both chosen elements lay on the free-edge of the TRAC boom. Thus, it is important to evaluate the singularity due to the free-edge effects, which cannot be evaluated by the global 2D model. In order to show those effects, a traction force of 1 N is applied to the structure. Figure 12 show the distribution of the out-of-plane stress components of the element A. Moreover, additional expansion elements are added on the thickness for convergence purposes (5LD3 in

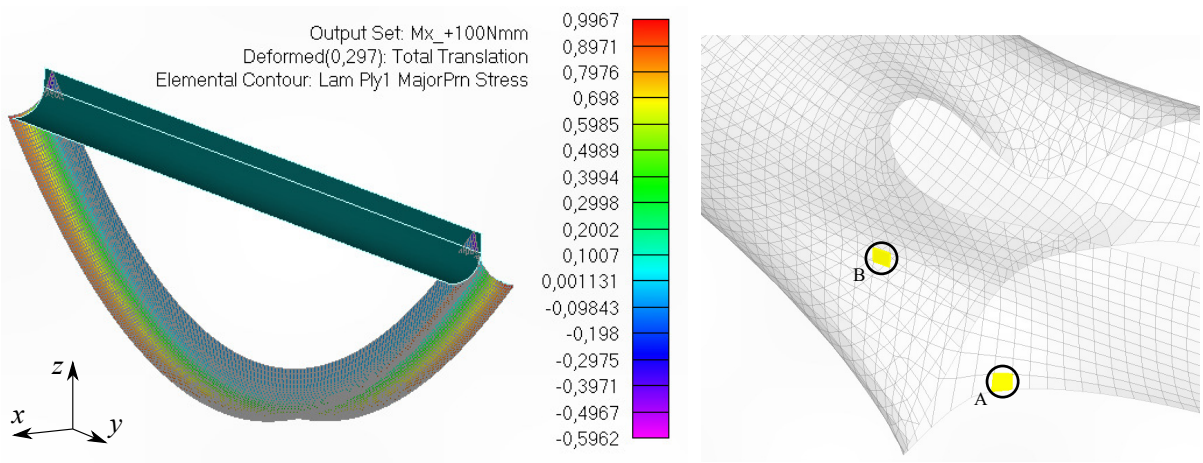

(a) (b)

Fig. 7 (a) Highest main stress distribution on the TRAC boom under $M_x = +100\,Nmm$. The results are shown for the first layer. (b) Element A on the vertical web and element B on the curved flange.

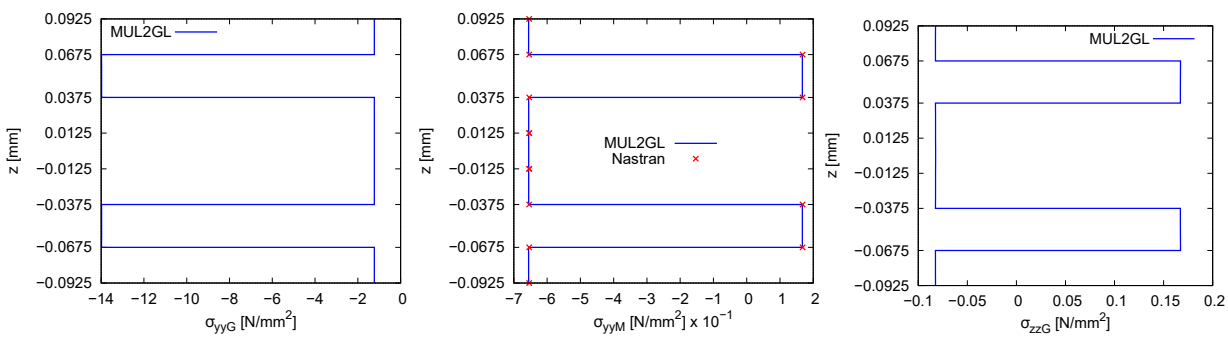

Fig. 8 Distribution of the σ_{yyG}, σ_{yyM} and σ_{zzG} on the centroid of the element A (vertical web, see Fig. 7).

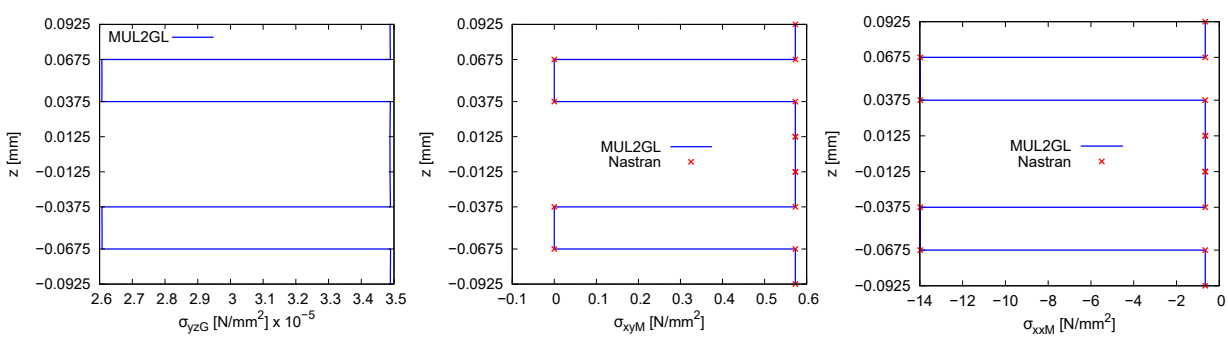

Fig. 9 Distribution of the σ_{yzG}, σ_{xyM} and σ_{xxM} on the centroid of the element A (vertical web, see Fig. 7).

particular). For the σ_{zzL}, peaks in the interfaces between CF and GFPW layers can be seen. For the shear components, the C_z^0 requirements [66] are satisfied and they are null at the thickness edges. Finally, 5LD3 approximation leads to highest values than LD3 for the σ_{xzL} and σ_{zzL}, whereas the result do not change for the σ_{yzL}. As far as the free-edge of the element B the results are reported in Fig. 13. The same conclusions can be drawn.

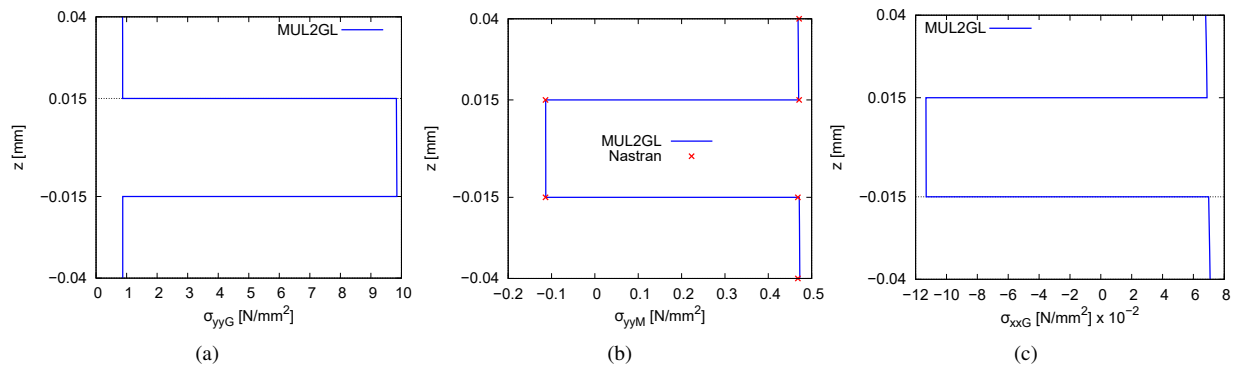

Fig. 10 Distribution of the σ_{yyG}, σ_{yyM} and σ_{xxG} on the centroid of the element B (curved flange, see Fig. 7).

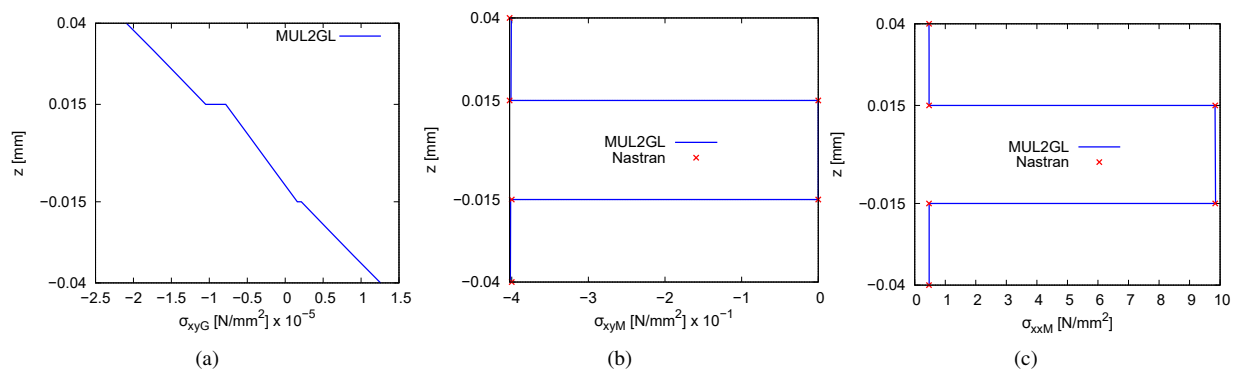

Fig. 11 Distribution of the σ_{xyG}, σ_{xyM} and σ_{xxM} on the centroid of the element B (curved flange, see Fig. 7).

3. Failure analysis

Furthermore, a failure analysis on the TRAC boom under a traction load T_y = 100 N is conducted, considering both centroid and free-edge stress distributions. The failure index is evaluated for the element B on the curved flange, see Fig. 7. Two failure criteria are considered, Hoffman and LaRC05. The material allowables are described in Table 2. As far as the Hoffman failure index is concerned, the results are shown in Fig. 14. Clearly, the indexes are higher if

	CF [67]	GFPW [68]
X_T	2700	452.37
X_C	1650	312.69
Y_T	55	452.37
Y_C	225	312.69
XY	100	69.76
XZ	100	69.76
YZ	32.26	44.83

Table 2 Material allowables in MPa.

the free-edge stress distributions are concerned. Moreover, the values are lower than 1, so the element is safe for the

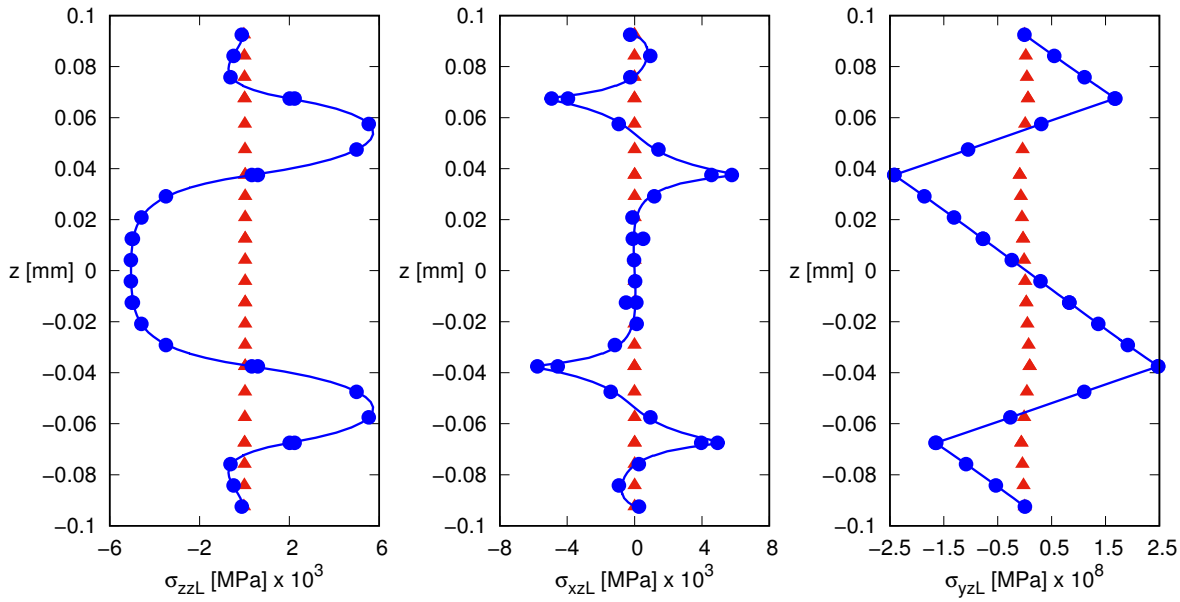

Fig. 12 Distribution of σ_{zzL}, σ_{xzL} and σ_{yzL} on the free-edge of the element A (vertical web, see Fig. 7). Triangles shows the results at the centroid of the element using LD3, circle and continuous line indicate the results at the free-edge using LD3 and 5LD3, respectively.

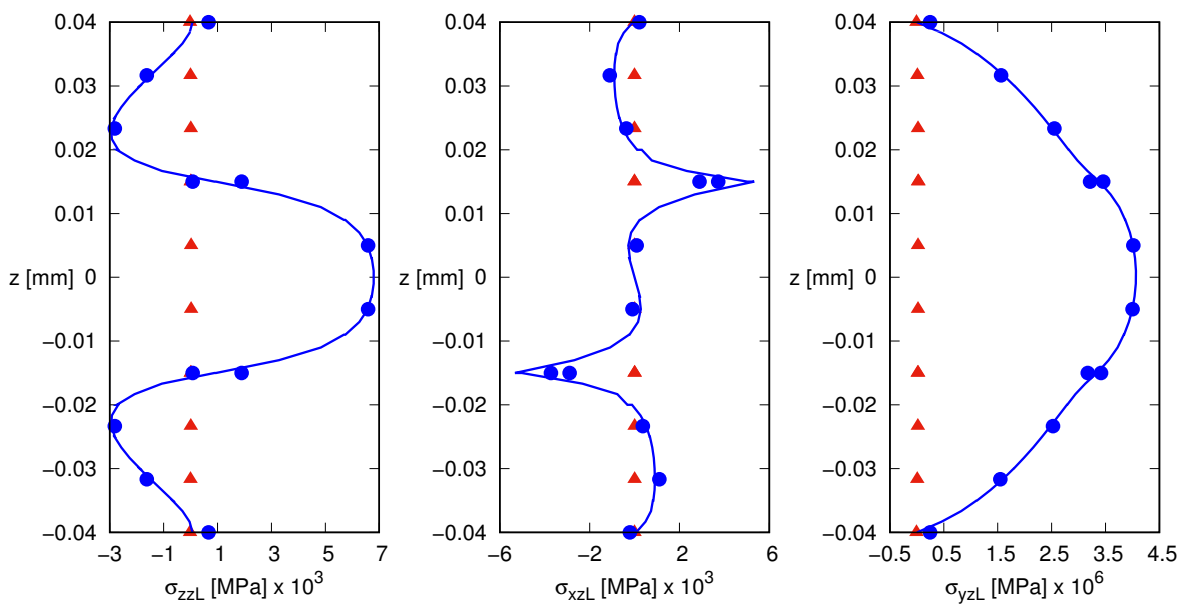

Fig. 13 Distribution of σ_{zzL}, σ_{xzL} and σ_{yzL} on the free-edge of the element B (curved flange, see Fig. 7). Triangles shows the results at the centroid of the element using LD3, circle and continuous line indicate the results at the free-edge using LD3 and 5LD3, respectively.

given external load (traction equals 100 N). Finally, Fig. 14(b) reports the failure index using the Larc05 criterion, for the fibres for the considered element. It can be pointed out that the highest values are in correspondence of the layers interfaces, highlighting the possible delamination between the layers. As far as the $FI_{Fiber,LaRC05}$ is concerned, the CF layers show the highest failure indexes.

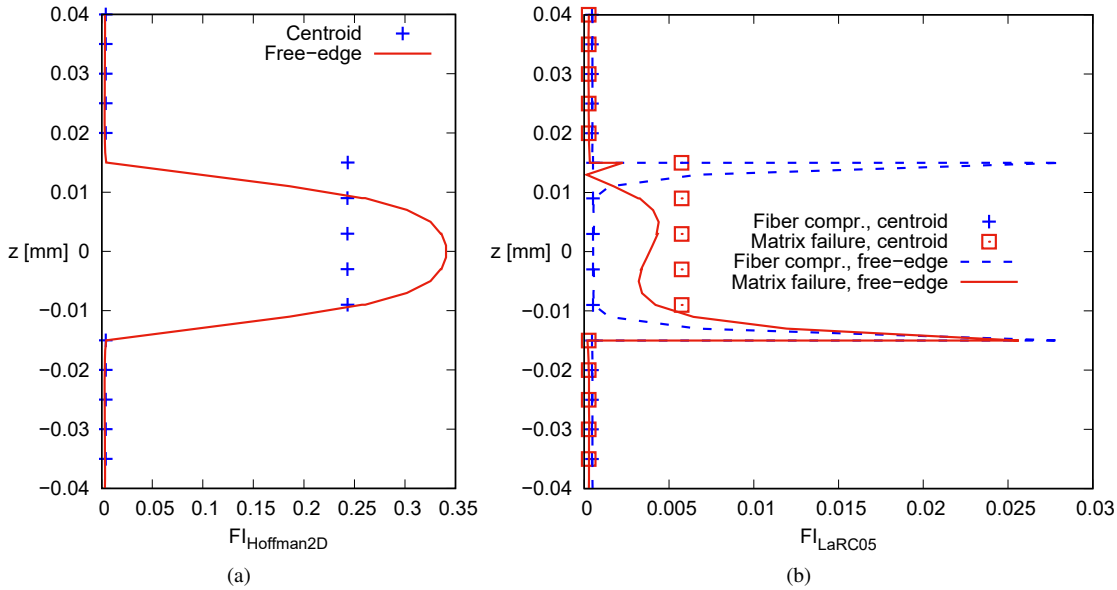

Fig. 14 Distribution of the $FI_{Hoffman2D}$, $FI_{Fiber,LaRC05}$ and $FI_{Matrix,LaRC05}$ for the element B on the curved flange of the TRAC boom.

B. Hinge tape-spring

The second study case deals with a composite tape-spring hinge. As in the previous case, particular elements of the global Nastran model are analyzed locally using refined theories. The considered structure is taken from [69] and [70], and its geometry, which is depicted in Fig. 15, involves a total length of 350 mm, a diameter of 38 mm and thickness of 0.2 mm. The hinge is built with a elliptical hole of length 110 mm and width 30 mm. The adopted material is made of

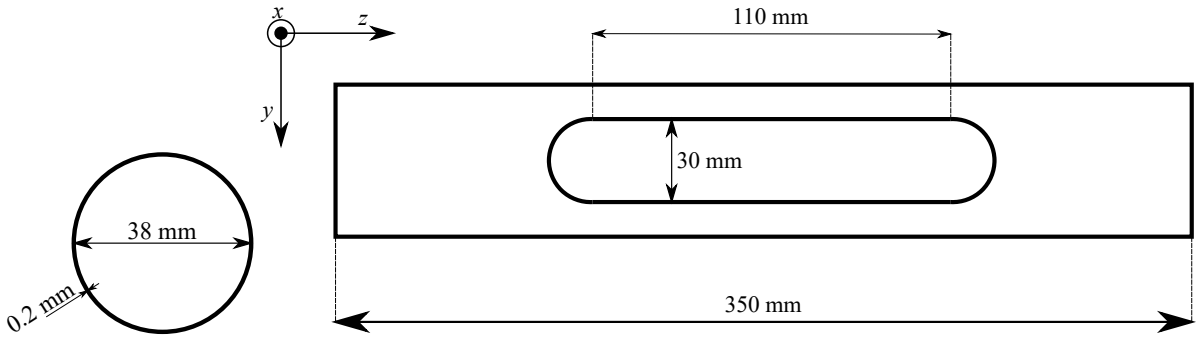

Fig. 15 Geometry of the tape-spring hinge.

carbon fibers (T300-1k) with an epoxy resin matrix (HexPly 913), whose material properties are reported in Table 3. The material is a weave, and it is approximated with two ±45 layers. The global nastran model was build using 8317

T300-1k/913 tow	
E_1	159520
$E_2 = E_3$	11660
$G_{12} = G_{13}$	3813
G_{23}	3961
$\nu_{12} = \nu_{13}$	0.27
ν_{23}	0.47
HexPly 913 resin	
E_m	3390
ν_m	0.41

Table 3 Material properties of the tape-spring hinge. Young and shear moduli are expressed in MPa.

2D elements (CQUAD and CTRIA) and 51186 DOFs. The structure is loaded with a moment M_x = 100 Nmm. The numerical results are shown in Fig. 16(a), where the obtained results (linear analysis) are compared with the nonlinear ones from [69]. As in the previous case, the two elements (see Fig. 16(b)) which suffer the highest stress, are analyzed with the local analysis. The chosen elements are highlighted in yellow. As far as the element A is concerned, the main

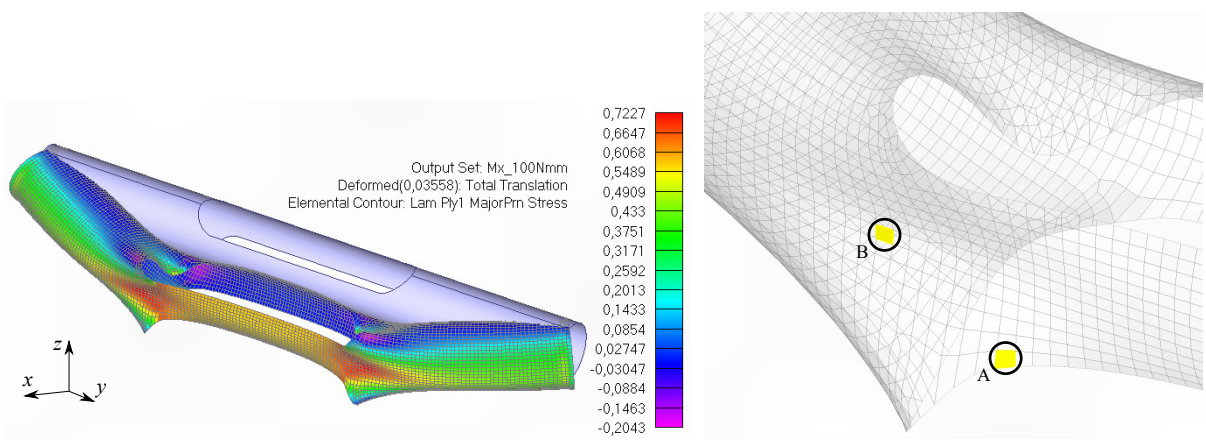

(a) (b)

Fig. 16 (a) Distribution of the stress on the tape-spring hinge subjected to M_z = 100 Nmm. (b) Starting from the left, the elements A and B are highligthed.

results on the stress distribution are shown in Figs. 17 and 18. As far as the element B is concerned, the results of the stress distributions show he same behavior as for the element A, i.e. Nastran model can not properly evaluate the through-the-thickness stress distribution of the in-plane components of the stresses.

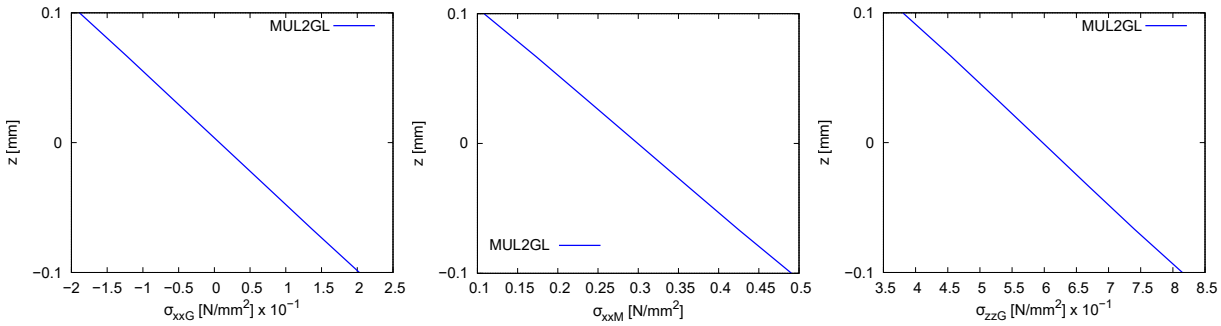

Fig. 17 Distribution of the σ_{xxG}, σ_{xxM} and σ_{zzG} on the centroid of the element A, see Fig. 16.

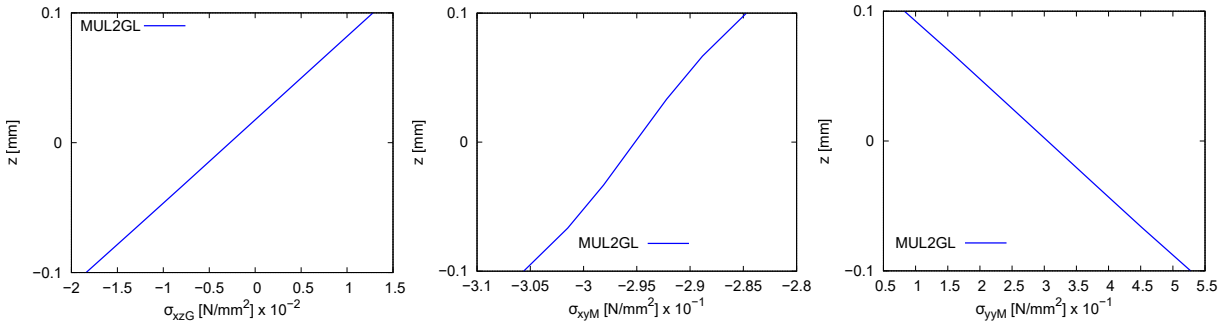

Fig. 18 Distribution of the σ_{xz}, σ_{xyM} and σ_{yy} on the centroid of the element A, see Fig. 16.

1. Failure analysis

For the failure analysis, Hoffman, Hashin3D e LaRC05 failure theories are considered. Those indeces are evaluated with an external moment equal to 4278 Nmm, since this load corresponds to the maximum moment acting on the tape-spring during the deployment. The failure indexes are evaluated on the centroid of the element A, so the aforementioned stress distributions are considered. The material allowables are reported in Table 4. Finally, Fig. 19

Tape-spring hinge allowables	
X_T	2005
X_C	1335
Y_T	68
Y_C	198
XY	150
XZ	150
YZ	28.39

Table 4 Material allowables of the tape-spring hinge. The values are taken from [71].

reports the distribution of the failure indexes using Hoffman, Hashin 3D and Larc05 criteria, respectively.

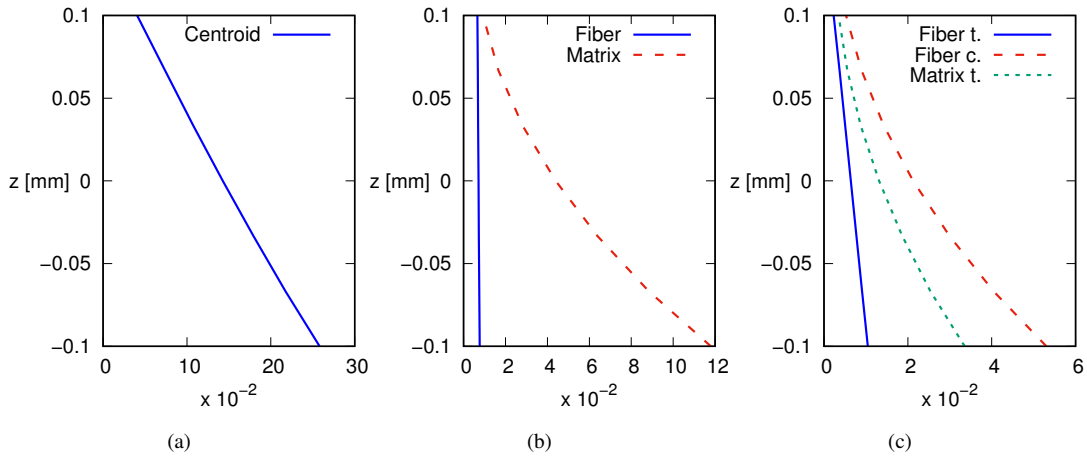

Fig. 19 Distribution of the Hoffman (a) , Hashin3D (b) and LaRC05 (c) failure indexes on the centroid of the element A, see Fig. 16. "t." stands for tension, "c." for compression.

C. Telescopic Tubular Mast

The final analysis case deals with the Telescopic Tubular Mast (TTM) [72]. The analyzed case is the deployed configuration, whose global Nastran model is shown in Fig. 20. The structure is made of 17 cylinders, with total length

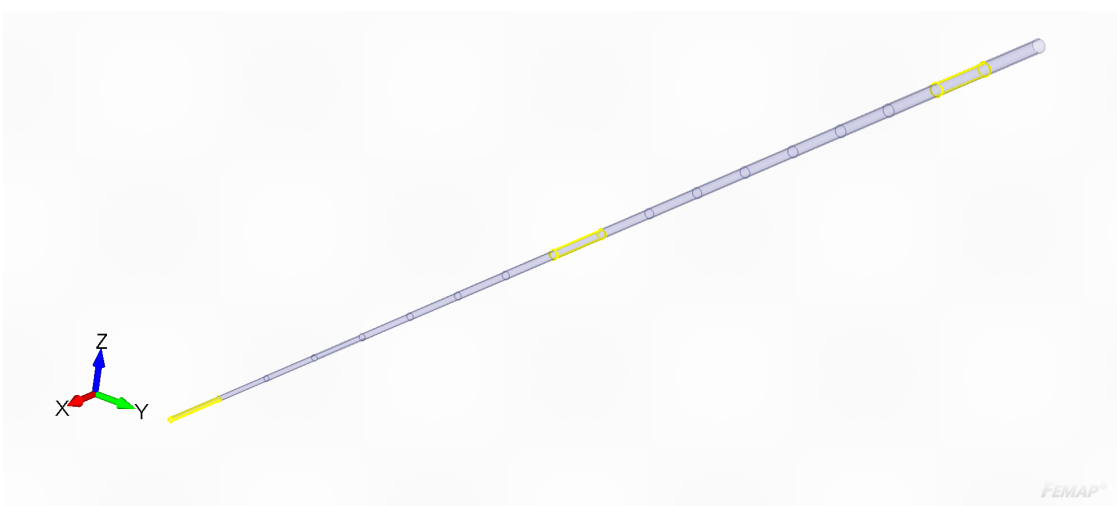

Fig. 20 Chosen cylinders for the local analysis.

equals 34.2 m. The diameter of the first cylynder is 31.8 cm, and this value decreases of 1.3 cm after each cylinder. Each cylinder has the same length 1.89 m and thickness 0.127 mm [73]. The adopted material is the P75/934, whose properties are reported in Table 5 and taken from [74]. The stacking sequence is described in Table 6. Finally, it must be pointed out that the structural stability and material debonding may play a key role in the design process of this structure, but in this work, the focus is put on the material failure onset mainly. The mathematical global model is made by 54000 CQUAD elements and 330816 DOFs. The side of the first cylinder is clamped, whereas the other is set

P75/934	
E_1	243000
$E_2 = E_3$	7200
$G_{12} = G_{13}$	3930
G_{23}	2410
$\nu_{12} = \nu_{13}$	0.33
ν_{23}	0.49

Table 5 Telescopic Tubular Mast material properties (Young and shear moduli in N/mm^2).

	Lamination	Thickness [mm]
First 2 cylinders (0,1)	[+45/-45/-45/+45]	0.508
Inner cylinders (2,...,16)	[+45/0/-45]	0.381
Last cylinder (17)	[+45/-45/0/0/0/0/-45/+45]	1.016

Table 6 Telescopic Tubular Mast stacking sequence and layers thickness.

free. The load acts in the transverse direction and it is equal to 1 N. Figure 21 shows the results of the static analysis versus the nonlinear results from [72]. As far as the local analysis is concerned, Fig. 22 shows the stress distribution for

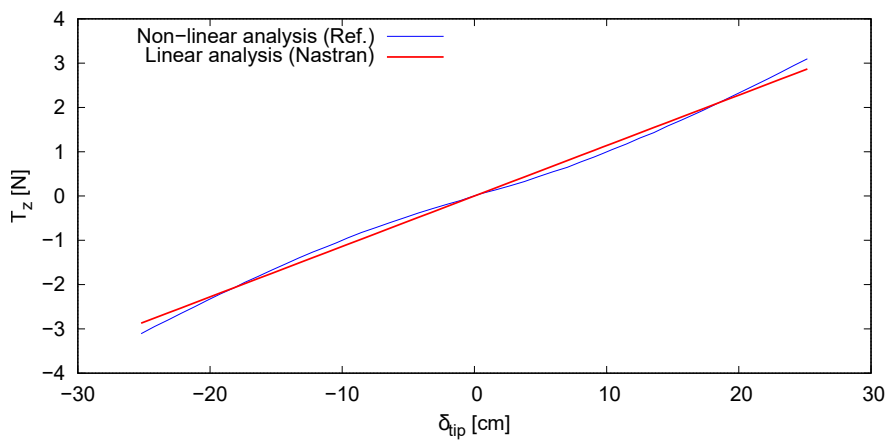

Fig. 21 Static results of the Telescopic tubular mast. Nonlinear solution coming from [72].

the first cylinder. The following conclusions can be drawn.

- The transverse stress component are three orders of magnitude lower than the in-plane ones;
- The C_z^0 requirements are partially satisfied. This aspect can be overcome by adding multiple through-the-thickness expansion elements, as described in the TRAC boom example;
- The Poisson effect is evident due to traction and compression of +45° and −45° layers.

For the elements of cylinders number 9 and 17, similar distributions are evaluated. Figure 23 reports the σ_{xyM} components of the ninth cylinder and the σ_{xxM} of the cylinder 17. The former highlights the limitation of the Nastran model to capture the shear stress component, whereas the latter shows the capability of the proposed global/local

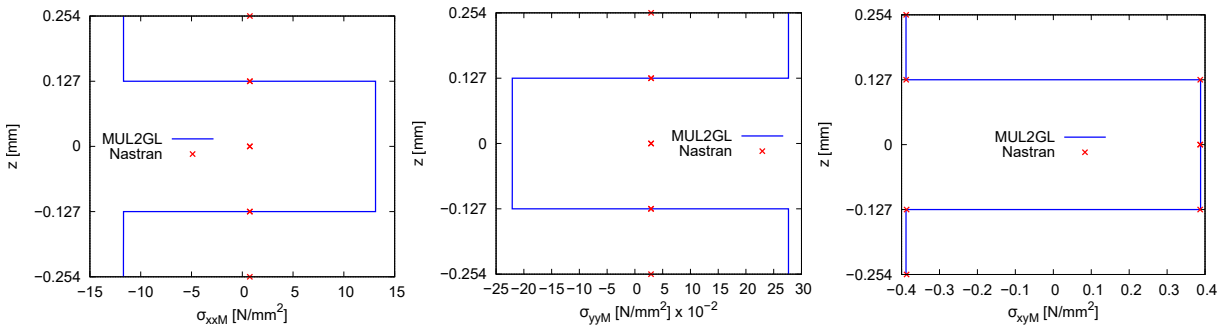

Fig. 22 Distribution of the σ_{xxM}, σ_{yyM} and σ_{xyM} on the centroid of first cylinder.

approach to accurately evaluate the in-plane stress over the plies.

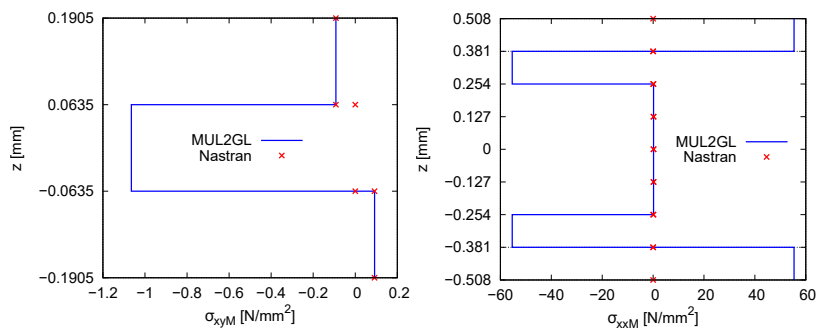

Fig. 23 Distribution of the σ_{xyM} and σ_{xxM} on the centroid of ninth cylinder and cylinder number 17, respectively

IV. Conclusions

In this work, a two-step global/local approach is employed for the structural analysis of deployable booms. The global analysis is carried out using the commercial software Nastran, whereas the local model is built by means of the Carrera Unified Formulation (CUF). Thanks to it, it is possible to build higher-order plate models of interesting local domains of the booms. The approach allowed to highlight the differences between the results obtained by the CUF approach and the results obtained by Nastran, which are generally based on the use of a classical theory. These differences are particularly evident for transverse stresses (obtained from Nastran through postprocessing), associated with phenomena that typically distinguish laminates from other structures (zig-zag and free-edge effects). Triangular Rollable and Collapsible (TRAC), tape-spring hinge and Telescopic Tubular Mast (TTM) were analyzed. For the TRAC boom, free-edge analyses were implemented, which highlighted the difference between the stress state in the centroid of the single element and the one obtained at its free edge. Moreover, the mesh refinement played a fundamental role in identifying the singularities of the transverse stresses on the free-edge, that would not have been absolutely possible using a classical theory, as commercial software operate. The differences between the global/lobal results and the ones obtained by Nastran are most evident for the tape-spring hinge and the TTM. In these cases, in fact, a greater deviation

is noted for the stresses calculated in the element plane.

References

[1] Leipold, M., Runge, H., and Sickinger, C., "Large SAR membrane antennas with lightweight deployable booms," *28th ESA Antenna Workshop on Space Antenna Systems and Technologies, ESA/ESTEC, Noordwijk, The Netherlands.*, 2005, pp. 1–8.

[2] Belvin, W. K., Straubel, M., Wilkie, W. K., Zander, M., Fernandez, J. M., and Hillebrandt, M., "Advanced deployable structural systems for small satellites," *NATO Specialists' Meeting AVT-257-RSM-041 "Best Practices for Risk Reduction for Overall Space Systems" organised by the Applied Vehicle Technology Panel, Zaragoza, Spain.*, 2016.

[3] Blanchard, L., Aridon, G., Falzon, F., Rémond, D., and Dufour, R., "A tape-spring hexapod for deployable telescopes: dynamics," *International Conference on Space Optics — ICSO 2006*, Vol. 10567, edited by E. Armandillo, J. Costeraste, and N. Karafolas, SPIE, Bellingham, Washington, USA, 2017, pp. 306 – 311. https://doi.org/10.1117/12.2308172, URL https://doi.org/10.1117/12.2308172.

[4] Dai, L., and Hu, L., "Kinematic Analysis and Model Fabrication of a Space Deployable Optical Baffle," *AIAA Journal*, Vol. 58, No. 3, 2020, pp. 1386–1396.

[5] Campbell, D., Barrett, R., Lake, M., Adams, L., Abramson, E., Scherbarthn, M., Welsh, J., Freebury, G., Beidleman, N., and Abbot, J., "Development of a novel, passively deployed roll-out solar array," *2006 IEEE Aerospace Conference, Big Sky, Montana, USA.*, 2006, pp. 1–9.

[6] Hoang, B., White, S., Spence, B., and Kiefer, S., "Commercialization of Deployable Space Systems' roll-out solar array (ROSA) technology for Space Systems Loral (SSL) solar arrays," *2016 IEEE Aerospace Conference, Big Sky, Montana, USA.*, 2016, pp. 1–12.

[7] Pehrson, N. A., Ames, D. C., Smith, S. P., Magleby, S. P., and Arya, M., "Self-deployable, self-stiffening, and retractable origami-based arrays for spacecraft," *AIAA Journal*, Vol. 58, No. 7, 2020, pp. 3221–3228.

[8] Leipold, M., Eiden, M., Garner, C., Herbeck, L., Kassing, D., Niederstadt, T., Krüger, T., Pagel, G., Rezazad, M., Rozemeijer, H., Seboldt, W., Schöppinger, C., Sickinger, C., and Unckenbold, W., "Solar sail technology development and demonstration," *Acta astronautica*, Vol. 52, No. 2-6, 2003, pp. 317–326.

[9] Banik, J., and Murphey, T., "Performance validation of the triangular rollable and collapsible mast," *24th Annual AIAA/USU Conference on Small Satellites, Logan, Utah, US*, 2010, pp. 1–8.

[10] Royer, F., and Pellegrino, S., "Ultralight ladder-type coilable space structures," *2018 AIAA Spacecraft Structures Conference, Kissimmee, Florida, USA.*, 2018, pp. 1–14.

[11] Seffen, K. A., and Pellegrino, S., "Deployment dynamics of tape springs," *Proceedings of the Royal Society of London. Series A: Mathematical, Physical and Engineering Sciences*, Vol. 455, No. 1983, 1999, pp. 1003–1048.

[12] Brinkmeyer, A., Pellegrino, S., and Weaver, P. M., "Effects of long-term stowage on the deployment of bistable tape springs," *Journal of Applied Mechanics*, Vol. 83, No. 1, 2016.

[13] Walker, S. J. I., and Aglietti, G., "Study of the dynamics of three dimensional tape spring folds," *AIAA journal*, Vol. 42, No. 4, 2004, pp. 850–856.

[14] Pica, G., Ciofaniello, L., Mattei, S., Santovito, M. R., and Gardi, R., "High-resolution deployable telescope for satellite applications," *Sensors, Systems, and Next-Generation Satellites VII*, Vol. 5234, SPIE, Bellingham, Washington, USA, 2004, pp. 531–538.

[15] Lai, C. Y., and Pellegrino, S., "Design and Testing of a 1.5 m Offset CRTS Demonstrator," *European Space Agency Contractor Report, Paris, France*, 2001.

[16] Seffen, K. A., and Pellegrino, S., "Deployment of a rigid panel by tape-springs," *Technical Report. Cambridge University Department of Engineering, Cambridge, UK*, 1997.

[17] Mallikarachchi, H. M. Y. C., and Pellegrino, S., "Quasi-Static Folding and Deployment of Ultrathin Composite Tape-Spring Hinges," *Journal of Spacecraft and Rockets*, Vol. 48, No. 1, 2011, pp. 187–198. https://doi.org/10.2514/1.47321.

[18] Yee, J. C., and Pellegrino, S., "Composite Tube Hinges," *Journal of Aerospace Engineering*, Vol. 18, No. 4, 2005, pp. 224–231. https://doi.org/10.1061/(ASCE)0893-1321(2005)18:4(224).

[19] Ye, H., Zhang, Y., Yang, Q., and Zhang, B., "Quasi-static analysis and multi-objective optimization for tape spring hinge," *Structural and Multidisciplinary Optimization*, Vol. 60, No. 6, 2019, pp. 2417–2430. URL www.scopus.com, cited By :2.

[20] Rimrott, F., and J., P., "Storable tubular extendible member: a unique machine element," *Machine Design*, Vol. 37, No. 28, 1965, pp. 156–165.

[21] Hazelton, C., Gall, K., Abrahamson, E., Lake, M., and Denis, R., "Development of a prototype elastic memory composite STEM for large space structures," *44th AIAA/ASME/ASCE/AHS/ASC Structures, Structural Dynamics, and Materials Conference, Norfolk, Virginia, USA.*, 2003.

[22] Higuchi, K., Watanabe, K., Watanabe, A., Tsunoda, H., and Yamakawa, H., "Design and evaluation of an ultra-light extendible mast as an inflatable structure," *47th AIAA/ASME/ASCE/AHS/ASC Structures, Structural Dynamics, and Materials Conference, Newport, Rhode Island, USA.*, 2006.

[23] Pellegrino, S., "Deployable structures in engineering," *Deployable structures*, Springer, Berlin, Germany, 2001, pp. 1–35.

[24] Crouch, D. S., "Mars Viking surface sampler subsystem," *25th conference on remote systems technology, Winter Garden, Florida, USA*, 1977, pp. 142–151.

[25] Murphey, T. W., and Banik, J., "Triangular rollable and collapsible boom," , 2011. USA Patent 7,895,795.

[26] Alhorn, D., Casas, J., Agasid, E., Adams, C., Laue, G., Kitts, C., and O'Brien, S., "Nanosail-d: The small satellite that could!" *Small Satellite Conference, Logan, Utah, US*, 2011.

[27] Biddy, C., and Svitek, T., "LightSail-1 solar sail design and qualification," *Proceedings of the 41st Aerospace Mechanisms Symposium*, Jet Propulsion Lab., National Aeronautics and Space Administration Pasadena, CA, USA, 2012, pp. 451–463.

[28] Betts, B., Spencer, D. A., Nye, B., Munakata, R., Bellardo, J. M., Wong, S. D., Diaz, A., Ridenoure, R. W., Plante, B. A., Foley, J. D., and Vaughn, J., "Lightsail 2: Controlled solar sailing using a CubeSat," *4th International Symposium on Solar Sailing*, JKyoto Research Park, Kyoto, Japan, 2017.

[29] Roybal, F., Banik, J., and Murphey, T., "Development of an elastically deployable boom for tensioned planar structures," *48th AIAA/ASME/ASCE/AHS/ASC Structures, Structural Dynamics, and Materials Conference, Honolulu, Hawaii, USA.*, 2007, p. 1838.

[30] Thomson, M., "Deployable and retractable telescoping tubular structure development," *The 28th Aerospace Mechanisms Symposium, Cleveland, OH, USA*, 1994.

[31] Royer, F., and Pellegrino, S., "Probing the Stability of Ladder-Type Coilable Space Structures," *AIAA Journal*, 2022, pp. 1–13.

[32] Kumar, H. C., V.and Dewangan, Sharma, N., and Panda, S. K., "Numerical prediction of static and vibration responses of damaged (crack and delamination) laminated shell structure: An experimental verification," *Mechanical Systems and Signal Processing*, Vol. 170, 2022, p. 108883.

[33] Dewangan, H. C., Sharma, N., and Panda, S. K., "Numerical nonlinear static analysis of cutout-borne multilayered structures and experimental validation," *AIAA Journal*, Vol. 60, No. 2, 2022, pp. 985–997.

[34] Hirwani, C. K., Mishra, P. K., and Panda, S. K., "Nonlinear steady-state responses of weakly bonded composite shell structure under hygro-thermo-mechanical loading," *Composite Structures*, Vol. 265, 2021, p. 113768.

[35] Babushka, I., Chandra, J., and Flaherty, J. E., *Adaptive computational methods for partial differential equations*, Vol. 16, SIAM, 1983.

[36] Szabó, B., and Babuška, I., *Finite Element Analysis: Method, Verification and Validation*, John Wiley & Sons, Hoboken, New Jersey, USA, 2021.

[37] Bathe, K.-J., *Finite element procedures*, Klaus-Jurgen Bathe, Watertown, MA, USA, 2006.

[38] Liu, Q., Jrad, M., Mulani, S. B., and Kapania, R. K., "Global/local optimization of aircraft wing using parallel processing," *AIAA Journal*, Vol. 54, No. 11, 2016, pp. 3338–3348.

[39] Moës, N., Dolbow, J., and Belytschko, T., "A finite element method for crack growth without remeshing," *International journal for numerical methods in engineering*, Vol. 46, No. 1, 1999, pp. 131–150.

[40] Fish, J., Pan, L., Belsky, V., and Gomaa, S., "Unstructured multigrid method for shells," *International Journal for Numerical Methods in Engineering*, Vol. 39, No. 7, 1996, pp. 1181–1197.

[41] Fish, J., "The s-version of the finite element method," *Computers & Structures*, Vol. 43, No. 3, 1992, pp. 539–547.

[42] Fish, J., and Markolefas, S., "Adaptive s-method for linear elastostatics," *Computer Methods in Applied Mechanics and Engineering*, Vol. 104, No. 3, 1993, pp. 363–396.

[43] Dhia, H. B., "Multiscale mechanical problems: the Arlequin method," *Comptes Rendus de l'Academie des Sciences Series IIB Mechanics Physics Astronomy*, Vol. 12, No. 326, 1998, pp. 899–904.

[44] Hu, H., Belouettar, S., and Potier-Ferry, M., "Multi-scale modelling of sandwich structures using the Arlequin method Part I: Linear modelling," *Finite Elements in Analysis and Design*, Vol. 45, No. 1, 2008, pp. 37–51.

[45] Akterskaia, M., Jansen, E., Hallett, S. R., Weaver, P. M., and Rolfes, R., "Progressive failure analysis using global-local coupling including intralaminar failure and debonding," *AIAA Journal*, Vol. 57, No. 7, 2019, pp. 3078–3089.

[46] Mao, K. M., and Sun, C. T., "A refined global-local finite element analysis method," *International journal for numerical methods in engineering*, Vol. 32, No. 1, 1991, pp. 29–43.

[47] Ransom, J. B., and Knight Jr., N. F., "Global/local stress analysis of composite panels," *Computers & structures*, Vol. 37, No. 4, 1990, pp. 375–395.

[48] Kapania, R. K., Haryadi, S. G., and Haftka, R. T., "Global/local analysis of composite plates with cutouts," *Computational Mechanics*, Vol. 19, No. 5, 1997, pp. 386–396.

[49] Haryadi, S. G., Kapania, R. K., and Haftka, R. T., "Global/local analysis of composite plates with cracks," *Composites Part B: Engineering*, Vol. 29, No. 3, 1998, pp. 271–276.

[50] Carrera, E., Filippi, M., Mahato, P. K., and Pagani, A., "Accurate static response of single-and multi-cell laminated box beams," *Composite Structures*, Vol. 136, 2016, pp. 372–383.

[51] Carrera, E., Cinefra, M., Petrolo, M., and Zappino, E., *Finite element analysis of structures through unified formulation*, John Wiley & Sons, Hoboken, New Jersey, USA, 2014.

[52] Kaleel, I., Petrolo, M., and Carrera, E., "Elastoplastic and progressive failure analysis of fiber-reinforced composites via an efficient nonlinear microscale model," *Aerotecnica Missili & Spazio*, Vol. 97, No. 2, 2018, pp. 103–110.

[53] Carrera, E., Kaleel, I., and Petrolo, M., "Elastoplastic analysis of compact and thin-walled structures using classical and refined beam finite element models," *Mechanics of advanced materials and structures*, Vol. 26, No. 3, 2019, pp. 274–286.

[54] Carrera, E., de Miguel, A. G., Filippi, M., Kaleel, I., Pagani, A., Petrolo, M., and Zappino, E., "Global-local plug-in for high-fidelity composite stress analysis in Femap/NX Nastran," *Mechanics of Advanced Materials and Structures*, Vol. 28, No. 11, 2021, pp. 1121–1127.

[55] "Global-local plug-in for high-fidelity composite stress analysis in ABAQUS," *Mechanics of Advanced Materials and Structures*, Vol. 28, No. 14, 2021, pp. 1445–1450.

[56] Zappino, E., Li, G., Pagani, A., and Carrera, E., "Global-local analysis of laminated plates by node-dependent kinematic finite elements with variable ESL/LW capabilities," *Composite Structures*, Vol. 172, 2017, pp. 1–14.

[57] Pagani, A., Carrera, E., de Miguel, A. G., Hasanyan, A., Pellegrino, S., Narravula, H. R., and Zappino, E., "Efficient analysis of geometrically nonlinear deployable thin shell structures using Carrera unified formulation,," *70th International Astronautical Congress (IAC), Washington D.C., USA.*., 2019.

[58] Pagani, A., Carrera, E., Hasanyan, A., and Pellegrino, S., "Advanced simulation and testing of composite TRAC longerons," *70th International Astronautical Congress (IAC), IAC CyberSpace Edition.*, 2020.

[59] Pagani, A., Augello, R., and Carrera, E., "Numerical simulation of deployable ultra-thin composite shell structures for space applications and comparison with experiments," *Mechanics of Advanced Materials and Structures*, 2022, pp. 1–13.

[60] Lifecycle, S. P., *NX Nastran User's Guide*, Management Software Inc, Plano, Texas, USA, 2014.

[61] Carrera, E., Giunta, G., and Petrolo, M., *Beam structures: classical and advanced theories*, John Wiley & Sons, Hoboken, New Jersey, USA, 2011.

[62] Reissner, E., "The effect of transverse shear deformation on the bending of elastic plates," *Journal of Applied Mechanics*, Vol. 12, 1945, pp. 69–77.

[63] Mindlin, R., "Influence of rotary inertia and shear flexural motion of isotropic, elastic plates." *Journal of Applied Mechanics*, Vol. 18, 1951, pp. 31–38.

[64] Leclerc, C., and Pellegrino, S., "Nonlinear elastic buckling of ultra-thin coilable booms," *International Journal of Solids and Structures*, Vol. 203, 2020, pp. 46–56.

[65] Pagani, A., Carrera, E., Hasanyan, A., and Pellegrino, S., "Advanced simulation ant testing of composite TRAC longerons," *71st International Astronautical Congress (IAC) – The CyberSpace Edition.*, 2020.

[66] Carrera, E., "Historical review of zig-zag theories for multilayered plates and shells," *Applied Mechanics Review*, Vol. 56, No. 3, 2003, pp. 287–308.

[67] Zhao, L., Wang, K., Ding, F., Qin, T., Xu, J., Liu, F., and Zhang, J., "A post-buckling compressive failure analysis framework for composite stiffened panels considering intra-, inter-laminar damage and stiffener debonding," *Results in Physics*, Vol. 13, 2019, p. 102205.

[68] Tang, J., Zhou, G., Wang, X., Li, C., and Silberschmidt, V. V., "Failure analysis of plain woven glass/epoxy laminates: Comparison of off-axis and biaxial tension loadings," *Polymer Testing*, Vol. 60, 2017, pp. 307–320.

[69] Mallikarachchi, H. M. Y. C., and Pellegrino, S., "Quasi-static folding and deployment of ultrathin composite tape-spring hinges," *Journal of Spacecraft and Rockets*, Vol. 48, No. 1, 2011, pp. 187–198.

[70] Mallikarachchi, H. M. Y. C., and Pellegrino, S., "Deployment dynamics of ultrathin composite booms with tape-spring hinges," *Journal of Spacecraft and Rockets*, Vol. 51, No. 2, 2014, pp. 604–613.

[71] Li, B., Ye, H., and Zhang, Y., "Failure analysis of composite tube hinge and optimization design," *IOP Conference Series: Materials Science and Engineering*, Vol. 531, IOP Publishing, Bristol, UK, 2019.

[72] Mobrem, M., and Spier, C., "Design and performance of the telescopic tubular mast," *41st Aerospace Mechanisms Symposium, Pasadena, CA, USA*, 2012.

[73] Lukez, R., "The use of graphite/epoxy composite structures in space applications," *Small Satellite Conference, Logan, Utah, USA*, 1987.

[74] Zhang, W., Binienda, W. K., and Pindera, M.-J., "Frictionless Contact of Multilayered Composite Half Planes Containing Layers With Complex Eigenvalues," , 1997. Lewis Research Center, Cleveland, OH, USA.

[75] Ochoa, O. O., and Reddy, J. N., "Finite element analysis of composite laminates," *Finite Element Analysis of Composite Laminates*, Springer, Berlin, Germany, 1992, pp. 37–109.

A. Additional details of the local model

Equation (3) reports the explicit function for the cubic interpolation expansion function used in this work over the thickness domain of the local layered model.

$$\begin{aligned} l_1 &= -\frac{9}{16}z^3 + \frac{9}{16}z^2 + \frac{1}{16}z - \frac{1}{16} \\ l_2 &= +\frac{27}{16}z^3 - \frac{9}{16}z^2 - \frac{27}{16}z + \frac{9}{16} \\ l_3 &= -\frac{27}{16}z^3 - \frac{9}{16}z^2 + \frac{27}{16}z + \frac{9}{16} \\ l_4 &= +\frac{9}{16}z^3 + \frac{9}{16}z^2 - \frac{1}{16}z - \frac{1}{16} \end{aligned} \tag{3}$$

As far as the shape function is concerned, cubic interpolation based on a 16-node Lagrange polynomial is employed.

The related polynomials are explained in Eq. (4).

$$
\begin{aligned}
L_1 &= \frac{(r-1)(1-9r^2)}{16} \times \frac{(s-1)(1-9s^2)}{16} & L_2 &= \frac{9(1-r^2)(1-3r)}{16} \times \frac{(s-1)(1-9s^2)}{16} \\
L_3 &= \frac{9(1-r^2)(1+3r)}{16} \times \frac{(s-1)(1-9s^2)}{16} & L_4 &= \frac{(r+1)(9r^2-1)}{16} \times \frac{(s-1)(1-9s^2)}{16} \\
L_5 &= \frac{(r+1)(9r^2-1)}{16} \times \frac{9(1-s^2)(1-3s)}{16} & L_6 &= \frac{(r+1)(9r^2-1)}{16} \times \frac{9(1-s^2)(1+3s)}{16} \\
L_7 &= \frac{(r+1)(9r^2-1)}{16} \times \frac{(s+1)(9s^2-1)}{16} & L_8 &= \frac{9(1-r^2)(1+3r)}{16} \times \frac{(s+1)(9s^2-1)}{16} \\
L_9 &= \frac{9(1-r^2)(1+3r)}{16} \times \frac{(s+1)(9s^2-1)}{16} & L_{10} &= \frac{(r-1)(1-9r^2)}{16} \times \frac{(s+1)(9s^2-1)}{16} \\
L_{11} &= \frac{(r-1)(1-9r^2)}{16} \times \frac{9(1-s^2)(1+3s)}{16} & L_{12} &= \frac{(r-1)(1-9r^2)}{16} \times \frac{9(1-s^2)(1-3s)}{16} \\
L_{13} &= \frac{9(1-r^2)(1-3r)}{16} \times \frac{9(1-r^2)(1-3r)}{16} & L_{14} &= \frac{9(1-r^2)(1+3r)}{16} \times \frac{9(1-r^2)(1-3r)}{16} \\
L_{15} &= \frac{9(1-r^2)(1+3r)}{16} \times \frac{9(1-r^2)(1+3r)}{16} & L_{16} &= \frac{9(1-r^2)(1-3r)}{16} \times \frac{9(1-r^2)(1+3r)}{16}
\end{aligned}
\tag{4}
$$

The relations are written in the natural coordinate system (r, s). Mathematical steps for the description in the physical domain can be found in [51]. 25 (5×5) cubic finite elements are used for the description of the mid-surface of the local element. An example of a 2-layer local model is depicted in Fig. 24.

The strain $\boldsymbol{\epsilon}$ and stress $\boldsymbol{\sigma}$ components are arranged as follows

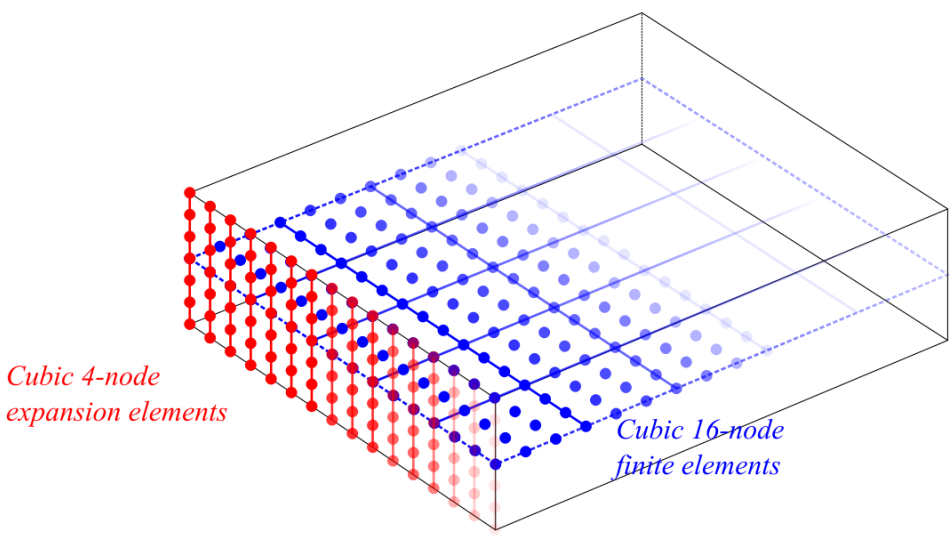

(a)

Fig. 24 2-layer local model.

$$
\boldsymbol{\sigma} = \left\{ \begin{array}{cccccc} \sigma_{xx} & \sigma_{yy} & \sigma_{zz} & \sigma_{xz} & \sigma_{yz} & \sigma_{xy} \end{array} \right\}^T, \quad \boldsymbol{\epsilon} = \left\{ \begin{array}{cccccc} \epsilon_{xx} & \epsilon_{yy} & \epsilon_{zz} & \epsilon_{xz} & \epsilon_{yz} & \epsilon_{xy} \end{array} \right\}^T \tag{5}
$$

In the case of small displacements with respect to a characteristic dimension the strain - displacement relations are

$$\boldsymbol{\epsilon} = \boldsymbol{D}\boldsymbol{u} \tag{6}$$

where D is the linear differential operator. For the sake of brevity matrix $\boldsymbol{D}$ is not reported here but can be easily found in [61]. The stress components can be attained by means of the Hooke's law

$$\boldsymbol{\sigma} = \boldsymbol{C}\boldsymbol{\epsilon} \tag{7}$$

where the material matrix $\boldsymbol{C}$ is

$$\mathbf{C} = \begin{pmatrix} C_{11} & C_{12} & C_{13} & 0 & 0 & C_{16} \\ C_{12} & C_{22} & C_{23} & 0 & 0 & C_{26} \\ C_{13} & C_{23} & C_{33} & 0 & 0 & C_{36} \\ 0 & 0 & 0 & C_{44} & C_{45} & 0 \\ 0 & 0 & 0 & C_{45} & C_{55} & 0 \\ C_{16} & C_{26} & C_{36} & 0 & 0 & C_{66} \end{pmatrix} \tag{8}$$

The material coefficients C_{ij} are functions of the elastic moduli along the longitudinal direction and the transverse directions of the fiber, the shear moduli, the Poisson ratios, and the fibre orientation angle. For the sake of brevity, their expressions are not given here but can be found in many reference texts, such as [75]. The governing equations are derived by applying the Principle of Virtual Displacements (PVD). For a static problem:

$$\delta L_{\text{int}} = \delta L_{\text{ext}} \tag{9}$$

where δL_{int} stands for the virtual variation internal work, δL_{ext} is the virtual variation of work done by the external loads. The virtual variation of the internal work can be expressed as

$$\delta L_{\text{int}} = \int_V \left(\delta \boldsymbol{\epsilon}^T \boldsymbol{\sigma}\right) \, \mathrm{d}V \tag{10}$$

and

$$\delta L_{\text{int}} = \delta \mathbf{q}_{sj}^T \mathbf{K}^{ij\tau s} \mathbf{q}_{\tau i} \tag{11}$$

where V is the volume of the local model and $\mathbf{K}^{ij\tau s}$ is the stiffness matrix in the form of a 3×3 fundamental nucleus (FN). The derivation FN is not reported here, but for the sake of completeness, it is described in [51]. However, the

terms $k_{xx}^{ij\tau s}$ and $k_{xy}^{ij\tau s}$ are given for clarity purpose.

$$
\begin{aligned}
k_{xx}^{ij\tau s} &= C_{11}\int_t F_\tau F_s \mathrm{d}z \int_\Omega N_{i,x}N_{j,x}\mathrm{d}\Omega + C_{44}\int_t F_{\tau,z}F_{s,z}\mathrm{d}z\int_\Omega N_iN_j\mathrm{d}\Omega \\
&+ C_{66}\int_t F_\tau F_s \mathrm{d}z \int_\Omega N_{i,y}N_{j,y}\mathrm{d}\Omega + C_{16}\int_t F_\tau F_s \mathrm{d}z \int_\Omega N_{i,x}N_{j,y}\mathrm{d}\Omega \\
&+ C_{16}\int_t F_\tau F_s \mathrm{d}z \int_\Omega N_{i,y}N_{j,x}\mathrm{d}\Omega \\
k_{xy}^{ij\tau s} &= C_{12}\int_t F_\tau F_s \mathrm{d}z \int_\Omega N_{i,y}N_{j,x}\mathrm{d}\Omega + C_{66}\int_t F_\tau F_s \mathrm{d}z \int_\Omega N_{i,x}N_{j,y}\mathrm{d}\Omega \\
&+ C_{45}\int_t F_{\tau,z}F_{s,z}\mathrm{d}z\int_\Omega N_iN_j\mathrm{d}\Omega + C_{26}\int_t F_\tau F_s \mathrm{d}z \int_\Omega N_{i,y}N_{j,y}\mathrm{d}\Omega \\
&+ C_{16}\int_t F_\tau F_s \mathrm{d}z \int_\Omega N_{i,x}N_{j,x}\mathrm{d}\Omega
\end{aligned}
\tag{12}
$$

It can be proven that all the components of $\mathbf{K}^{ij\tau s}$ can be derived from Eq. (12) by permutations. Given the definition of δL_{int} and δL_{ext} (the latter can be found in [61]) and introducing them in Eq. 9, the classical static problem arises.